RSC Advances

PAPER

View Article Online
View Journal | View Issue

Cite this: *RSC Adv.*, 2023, **13**, 4173

A facile synthesis of highly efficient In_2S_3 photocatalysts for the removal of cationic dyes with size-dependent photocatalysis†

Chaofan Zheng,‡[a] Ziyao Wang,‡[a] Jialong Yuan,[a] Qingfeng Xu,[a] Haixin Li,[a] Xiaoyi Lu,[a] Jiangang Gao*[ab] and Wenjin Yue *[ab]

In this study, a 3D thornball-like hierarchical β-In_2S_3, displaying extremely rapid photodegradation of cationic dyes, was synthesized by a facile method. The formation of a uniform thornball-like structure depended on the microwave reaction method and citric acid as the pH regulator. The size of In_2S_3 was easily adjusted by changing the microwave irradiation time from 5 min to 15 min. The morphology, structure, composition, energy level, charge separation, and surface properties of different-sized In_2S_3 were characterized. The results showed that In_2S_3 synthesized in 10 min (In_2S_3-10) displayed optimal interface property for the electron–hole separation, maximum hydrophilia with most surface negative charges for the surface adsorption, contributing to the complete photodegradation of rhodamine B (RhB) in just 25 minutes of visible light illumination. The photodegradation path of RhB was speculated with four possible paths, including the processes of de-ethylation, open-ring of xanthene, and rupture of carbon–carbon bonds up to the decomposition into small molecules. Finally, the reusability of In_2S_3-10 was tested, obtaining nearly 96% photodegradation efficiency after sequential 5 cycles.

Received 9th November 2022
Accepted 16th January 2023

DOI: 10.1039/d2ra07108h

rsc.li/rsc-advances

1 Introduction

Recently, air and water pollution are major environmental problems threatening human health. The most ideal and feasible strategy to solve the problem is semiconductor photocatalytic technology. Common semiconductor photocatalysts such as TiO_2, CdS, ZnS have been studied previously.[1] However, these photocatalysts either do not have the high efficiency as TiO_2 or[2] do not have high stability as CdS and ZnS.[3,4] Therefore, it is important to synthesize practical photocatalysts for application in photocatalytic technology. Normally, the synthesis strategy involves structural and compositional optimization because the photocatalysis is strongly dependent on crystal morphologies and structural features at the nanometer level.[5]

Indium sulphide is a nontoxic III–VI group semiconductor, as the most stable crystal phase, β-In_2S_3 displays the narrow bandgap of 1.9–2.3 eV.[6] Many inherent vacancies are conducive to forming the transition defect zones in β-In_2S_3, contributing to the excellent light-harvesting ability in visible light range.[7] Ordinary nano-photocatalysts with large specific surface areas have numerous surface active sites; however, the easy agglomeration results in considerable surface active sites being ineffective.[8] Micro/nano hierarchical photocatalysts can retain the advantages of nano-photocatalysts by avoiding agglomeration effectively, for example, their large interface area not only affords abundant active sites for better contact of pollutant with catalyst but also contribute to the high separation of electron–hole pairs.[5] Previous reports have confirmed that the application of 3D ZnO in the photodegradation of methyl orange displayed higher performance than ZnO fragments.[9] Therefore, it is suggested that micro/nano hierarchical In_2S_3 has special advantages in the photocatalysis. Previously, micro/nano hierarchical In_2S_3 has been prepared by a solvothermal method[10–15] or a hot injection method.[16,17] However, the solvothermal reaction requires high temperature as 150–195 °C and a long reaction time of 2–30 h, and the hot injection method demands complicated reagents or surfactant (glycerinum, myristic acid, and octadecene) to react under an inert gas atmosphere at high temperature.

Based on the direct coupling of microwave energy with a reactant, the microwave irradiation method presents a very fast reaction rate in material synthesis.[18] The extremely fierce reaction driven by microwave energy contributed to the advantageous three-dimensional growth of the product.[19] Thus, products tend to aggregate into hierarchical clusters with more uniform size distribution and more complete crystal

[a]*School of Chemical and Environmental Engineering, Anhui Polytechnic University, Wuhu, 241000, P.R. China. E-mail: gaojiangang@ahpu.edu.cn*

[b]*Anhui Laboratory of Clean Energy Materials and Chemistry for Sustainable Conversion of Natural Resources, Wuhu, 241000, P.R. China. E-mail: yuewenjin_79@163.com*

† Electronic supplementary information (ESI) available. The details on Photocatalysis experiments (S1), Electrochemical measurements (S2) and Calculation of band edge potential based on empirical equation and *C–V* measurement (S3). See DOI: https://doi.org/10.1039/d2ra07108h

‡ These authors contributed equally to this work.

morphology. By changing the reaction parameters, such as temperature, time, or microwave power, the size and morphology can be adjusted easily to obtain the controllable preparation of the photocatalysts with excellent surface properties for high photocatalysis. Previously, preparation of In_2S_3 nanoflowers by PVP-assisted microwave irradiation method,[19] dandelion flower-like In_2S_3 by the microwave solvothermal method[20] and dendrites-type In_2S_3 by the microwave irradiation method under nitrogen atmosphere[21] have been reported. In these reactions, long-chained surfactants, high reaction temperature, or complicated process are needed, resulting in the following disadvantages inevitably. (1) The surfactant covers the surface of In_2S_3 to generate the charge transfer obstacle between the photocatalysts and organic pollutes; (2) high reaction temperature and the complicated process lead to increased environmental contamination and synthesis cost. Therefore, how to obtain desired 3D micro/nano hierarchical In_2S_3 by a facile method requires further exploration.

In this work, we put forward a facile microwave strategy to synthesize surfactant-free thornball-like hierarchical In_2S_3. All reagents are nontoxic with deionized water as the solvent, and the reaction is achievable as fast as 5 min at the low temperature of 90 °C. Furthermore, different-sized In_2S_3 were synthesized easily by adjusting the microwave reaction time, which was applied in the photodegradation of rhodamine B (RhB) to obtain size-dependent photocatalysis. Mid-sized In_2S_3 (In_2S_3-10) displayed excellent photocatalysis, which was much better than that previously reported In_2S_3 using a similar structure,[22–26] confirming its potential application in the treatment of environmental pollutants. The corresponding explanation was given based on the synergistic effect from the surface adsorption of dye molecules followed by the oxygenolysis of active specifies.

2 Experimental

2.1 Chemicals

Indium chloride tetrahydrate ($InCl_3 \cdot 4H_2O$, AR), thioacetamide (TAA, AR), citric acid (CA, AR), oxalic acid (AR), ethanol (AR), rhodamine B (RhB, AR), crystal violet (CV, AR), malachite green (MG, BS), methyl orange (MO, Ind), congo red (CR, Ind), acid red (AR, Ind), isopropanol (IPA, AR), triethanolamine (TEOA, AR) and benzoquinone (BQ, AR) were purchased from the Sinopharm Chemical Reagent Co, Ltd.

2.2 Synthesis of In_2S_3 micro/nanoparticles

60 mL mixed solution containing $InCl_3 \cdot 4H_2O$ (0.025 mol L^{-1}) and TAA (0.1 mol L^{-1}) was adjusted to pH = 2.0 by CA. Then, the mixed solution was transferred to an XH-MC-1 microwave synthesis reactor to react at 90 °C, 200 W for 5, 10, and 15 min. After the reaction was completed, the products were centrifuged at 10 000 rpm for 10 min followed by washing and drying to obtain yellow powders, named In_2S_3-5, In_2S_3-10, and In_2S_3-15. As a comparison, the synthesis conditions of In_2S_3-10 were changed as follows: (1) chemical bath deposition (CBD) was used instead of the microwave method; (2) no pH regulator was used; (3) oxalic acid instead of CA was used as a pH regulator.

2.3 Photocatalysis experiments

In_2S_3-5, In_2S_3-10, and In_2S_3-15 were used to carry out the photocatalysis experiments (S1 in the ESI†). To detect the active species in the photodegradation of RhB with In_2S_3-10, IPA (1 mM), TEOA (1 mM), and BQ (1 mM) were used as the scavengers for $^{\bullet}OH$, h^+, and $^{\bullet}O_2^-$, respectively, by adding them in the system. The reusability of In_2S_3-10 was tested using the equivalent photocatalyst in every experiment.

2.4 Characterization

The morphology of products was studied by scanning electron microscopy (FEI Sirion 200) and transmission electron microscopy (JEOL-2010). The crystal phase was measured using an X-ray diffractometer (MXP18AHF) with monochromated CuKα radiation ($\lambda = 1.54056$ Å). The optical measurements were performed by UV-vis diffused reflectance spectroscopy (UV 2550 spectrophotometer) and fluorescence spectra (an F-4500 spectrofluorometer) with an excitation wavelength of 218 nm. The photoelectrochemical measurements including cyclic voltammetry (*C–V*), linear sweep voltammetry (LSV), transient photocurrent-time (*I–t*) curves, and electrochemical impedance spectroscopy (EIS) were studied using a CHI-660C electrochemical workstation (S2 in the ESI†). The specific surface areas were measured on the NOVA 2000e instrument with Brunauer–Emmett–Teller (BET) method, and the pore-size distribution was estimated using the Barrett–Joyner–Halenda (BJH) method. The measurement of zeta potential was performed on Brookhaven 90 plus zeta potential analyser. The water contact angles were measured with a Kino SL250 contact angle meter (USA Kino Industry Co. Ltd). FT-IR spectra were recorded on a Nicolet Magna-IRTM 750 spectrometer. The photodegradation products were identified by liquid chromatography-mass spectrometry (Shimadzu LCMS-8030) with a mass scanning range of 50–450 *m*/*z*, similar to that reported in our previous paper.[27,28]

3 Results and discussion

3.1 Influence of synthetic condition on the morphology of In_2S_3

Fig. 1 shows the influence of the reaction method and the category of pH regulator. Fig. 1a and b show SEM images of In_2S_3 synthesized using CBD and the microwave method, respectively. With the CBD method, two morphologies of In_2S_3 including thornball-like structure with the size of 1–1.5 μm and irregular aggregated particles (as shown in a white dotted line) generated, however, the microwave method resulted in the formation of 500–600 nm sized uniform thornball-like structures. Furthermore, we changed the pH regulator, compared to that with CA as a pH regulator (Fig. 1b), extremely small-sized spherical nanoparticles were formed without the pH regulator (Fig. 1c), however, the oxalic acid regulator led to the formation of a flower-like structure with the size of 1 μm. Obviously, the microwave method contributed to the generation of

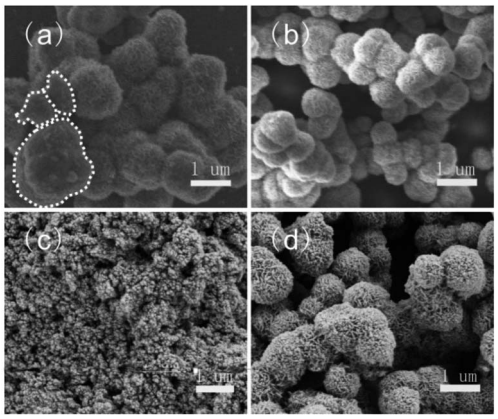

Fig. 1 SEM images of In_2S_3 synthesized using different reaction methods as CBD (a) and microwave method (b–d), and different pH regulators, such s as CA (a and b), none (c), and oxalic acid (d).

monomorphic morphology, CA promoted the production of thornball-like structures. The formation of thornball-like In_2S_3 was possibly based on the followings. Firstly, In^{3+} coordinated with CA to form the In-CA compound. With the hydrolysis of TAA to release H_2S, the In-CA compound was attacked by H_2S to produce the In_2S_3 crystal nuclei followed by the oriented growth into nanoflakes. After more and more nanoflakes were formed, they tended to aggregate into hierarchical clusters as the microwave reaction promoted to three-dimensional growth of the products.[19]

3.2 Characterization

3.2.1 Morphologies, structures, and composition. Fig. 2 shows the SEM morphology and corresponding EDS spectrum (with the gold-spraying treatment) of In_2S_3 synthesized for different microwave reaction time. In_2S_3-5 displayed the thornball-like structure with a size of 400–500 nm, which was assembled by thin nanoflakes (Fig. 2a). The EDS spectrum confirmed the presence of In, S, C, O, and Au elements in the product with an In/S ratio of 0.692 (Fig. 2b). The high content of C originated from the presence of CA on its surface. In_2S_3-10 displayed almost the same morphology except the size increased to 500–600 nm (Fig. 2c). The EDS spectrum showed an increase in the In/S ratio of 0.717 and decreased content of carbon (Fig. 2d). Furthermore, the size obviously increased to 700–800 nm in In_2S_3-15 (Fig. 2e). The In/S ratio further increased to 0.728 and the content of carbon decreased further (Fig. 2f). Clearly, microwave reaction promoted the formation of micro/nano thornball-like In_2S_3, rapidly, the increase of the reaction time hardly resulted in the change in morphology, just promoting the increase in the size. Moreover, the increased time resulted in the increased ratio of In/S and decreased the content of carbon, which was originating from the gradual decomposition of In-CA composites for the transformation into In_2S_3.

The phase structure of the products was characterized from powder XRD (Fig. 3a). The diffraction peaks at $2\theta = 27.4°$, 33.2°, 43.6° and 47.7° matched with (109), (0012), (1015) and (2212) crystal planes of tetragonal β-In_2S_3 ($a = b = 7.619$ A, $c = 32.329$ A, JCPDS PCPDFWIN #25-0390), respectively.[7,19] With the reaction time prolonging, the full-width half maximum (FWHM) of (2212) peak decreased (FWHM = 2.5°, 2.2° and 1.5° for In_2S_3-5, In_2S_3-10, and In_2S_3-15, respectively), implying that the average size of In_2S_3 increased. Additionally, the appearance of the sharper peaks in large-sized In_2S_3 indicated better crystallinity of the products.

To characterize the product composition more accurately, XPS spectra were obtained. The survey spectrum displayed the existence of In, S, C, and O elements in three In_2S_3 samples (Fig. 3b). The oxygen peak originated from the adsorption of O_2 or H_2O molecules in the atmosphere onto the samples, while the carbon peak was due to the residual CA molecules and CO_2

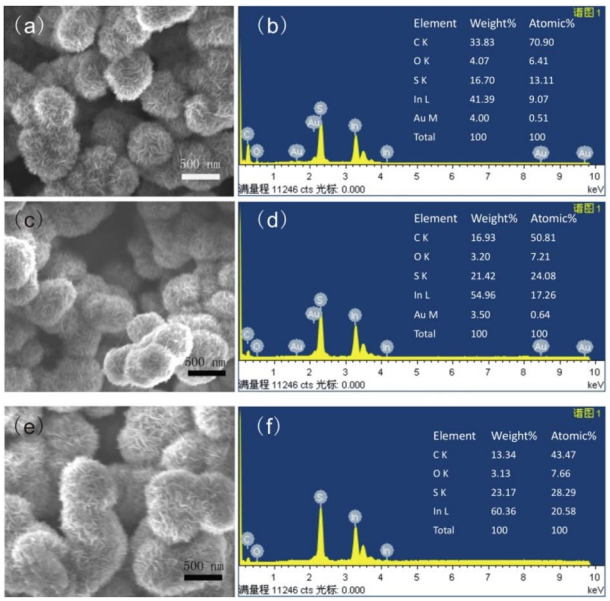

Fig. 2 SEM (a) and EDS (b) of In_2S_3-5, SEM (c) and EDS (d) of In_2S_3-10, SEM (e) and EDS (f) of In_2S_3-15.

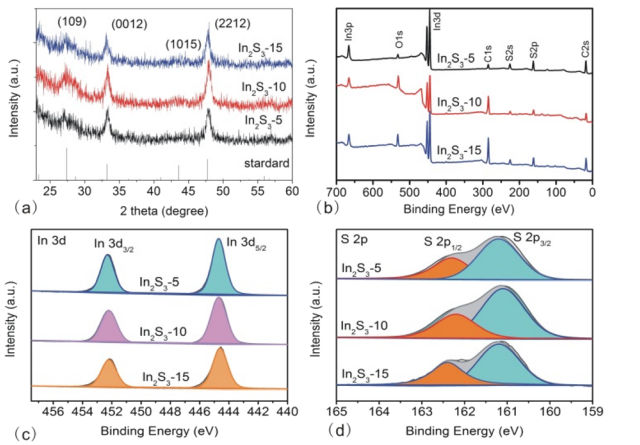

Fig. 3 XRD (a), XPS survey (b), In spectrum (c), and S spectrum (d) of In_2S_3-5, In_2S_3-10, and In_2S_3-15.

from the atmosphere.[29] To obtain information on the valence states and binding energy, In and S spectra were collected. There were two peaks located at 445 eV and 452 eV in In 3d spectrum (shown in Fig. 3c), which corresponded to In $3d_{5/2}$ and In $3d_{3/2}$, respectively. The spin–orbit separation of In was 7 eV, indicating that In was present in the form of In(III). In the S 2p spectrum, two peaks at 161 eV and 162 eV related to S $2p_{3/2}$ and S $2p_{1/2}$ could be seen (shown in Fig. 3d). The spin–orbit separation of 1 eV suggested that S existed as S^{2-} in the In_2S_3.[22]

Fig. 4 shows TEM images of three In_2S_3. In_2S_3-5 displayed a 400–500 nm spherical structure assembled by 10–20 nm nanoflakes. The nanoflakes interleaved to form thornball-like structures with irregular edges (Fig. 4a). In_2S_3-10 presented similar morphology to In_2S_3-5 except for the increased size to 600–700 nm (Fig. 4b), and the size of In_2S_3-15 further increased to 700–800 nm (Fig. 4c). Obviously, as the reaction time increased, the size of the as-synthesized In_2S_3 increased largely. HRTEM images showed the interplanar spacing of 0.324 (or 0.323) nm and 0.194 nm corresponding to (109) and (2212) planes of β-In_2S_3. The polycrystalline rings, as indicated in SAED, resulted from (109), (2212), and (419) planes of tetragonal β-In_2S_3.

3.2.2 Energy level. To obtain the information on the energy level for In_2S_3, we firstly investigated UV-vis DRS of different-sized In_2S_3 (Fig. 5a), they absorbed visible light within 200–650 nm with the absorption band edge around 610–630 nm. On the basis of DRS results, the optical bandgap (E_{g-O}) of In_2S_3 was calculated using the Tauc plot method[30] (inset to Fig. 5a), which was 2.12–2.20 eV for three In_2S_3 (as shown in Table 1). Obviously, with the size of In_2S_3 increasing, the bandgap decreased with the absorption band edge red-shifted. Small-sized In_2S_3 had a large bandgap, which was unhelpful for light-harvesting, however, the large specific surface area contributed to strong light reflection and scattering ability. Comprehensively, In_2S_3-10 displayed complementary light absorption, reflection, and scattering ability, obtaining the maximum light-harvesting ability. Next, we calculated E_{VB} (valence band edge potential) and E_{CB} (conduction band edge potential) according to the empirical equation[23] (S_3 in the ESI†). Obviously, with the size of In_2S_3 increasing, E_{VB} decreased and E_{CB} increased gradually (as shown in Table 1), originating from the quantum size effect.[31]

C–V measurement is an effective method to obtain the energy level of nanoparticles.[28,29] Based on the quantitative correlation between the band edge potential with the onset potential of the oxidation and reduction peaks (S3 in the ESI†), we obtained the ionization potential (IP) and the electron affinity (EA). From Fig. 5b, E_{ox} negatively shifted gradually from In_2S_3-5 to In_2S_3-15, resulting in decreased IP, however, E_{ox} positively shifted gradually for increased EA. With the size of In_2S_3 increasing, the electrochemical bandgap ($E_{g-E} = IP - EA$) decreased gradually.

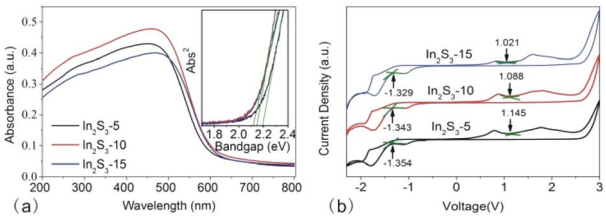

Fig. 5 UV-vis DRS (a) and *C–V* curve (b) of In_2S_3-5, In_2S_3-10, and In_2S_3-15, the inset to (a) is the spectrum, which shows the determination of bandgap by the direct bandgap method.

3.2.3 Charge separation. PL spectra that resulted from the recombination of the photoexcited charge carriers also reflect the charge separation ability. Fig. 6a shows the spectra of different-sized In_2S_3 with the emission peaks appearing at 570–580 nm, near the peak at 587 nm reported in the literature.[32] Different from In_2S_3-10 and In_2S_3-15, an obvious blue-shifted peak in In_2S_3-5 attributed to the quantum size effect was observed. Among the three samples, In_2S_3-10 presented the lowest emission peak intensity, indicating that the electrons and holes were not easy to recombine.[33] It is well-known that the electron–hole recombination rate is connected closely with the surface states. Small-sized nanoparticles with a large special surface area are helpful to afford the interface for electron–hole separation, however, the presence of more surface atoms producing surface defects inevitably acted as the recombination centre.[34] In_2S_3-10 balanced the effect originating from special surface area and surface defects, therefore, obtaining the highest electron–hole separation efficiency.

The photoelectrochemical measurements are useful to probe electron–hole separation. Fig. 6b showed LSV curves of In_2S_3 particles. The increase in the current density of In_2S_3-10 was significantly higher than that of In_2S_3-5 and In_2S_3-15, indicating that In_2S_3-10 had a faster transfer rate of the photogenerated

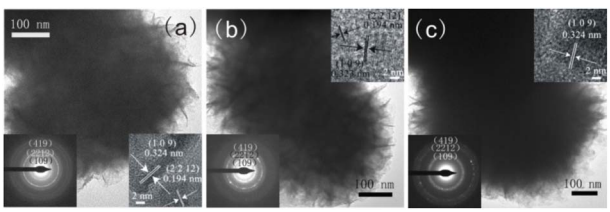

Fig. 4 TEM of In_2S_3-5 (a), In_2S_3-10 (b), and In_2S_3-15 (c), the insets are HRTEM and SAED of three samples, respectively.

Table 1 The corresponding data of energy level for different In_2S_3 based on optical and electrochemical methods[a]

sample	In_2S_3-5	In_2S_3-10	In_2S_3-15
E_{g-O} (V)	2.20	2.15	2.12
E_{VB-cal} (eV)	1.30	1.28	1.26
E_{CB-cal} (eV)	−0.90	−0.88	−0.86
E_{ox} (V)	0.651	0.647	0.602
E_{VB-CV} (eV)	1.304	1.300	1.255
E_{red} (V)	−1.402	−1.364	−1.345
E_{CB-CV} (eV)	−0.749	−0.711	−0.692
E_{g-E} (V)	2.053	2.011	1.947

[a] Note: E_{ox} and E_{red} represent the onset potential of the oxidation peak and reduction peak in *C–V* curves.

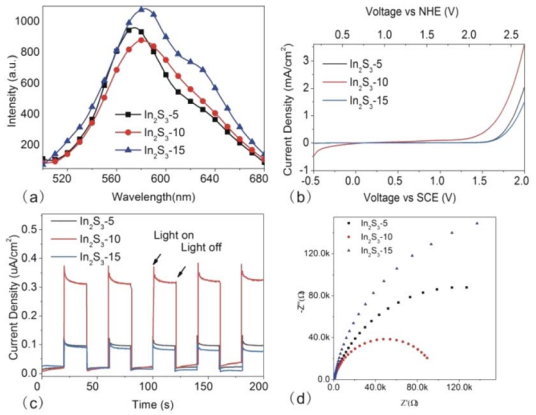

Fig. 6 PL spectra (a), LSV (b), *I*–*t* (c) and EIS (d) curves of In_2S_3-5, In_2S_3-10 and In_2S_3-15.

electrons. Moreover, we compared the onset potential of three samples, which represented the position of the Fermi level.[33] In_2S_3-10 with the low onset potential suggested the low potential for the photoanode to integrate with the photocathode, contributing to the efficient separation of the photogenerated carriers.

Fig. 6c shows the transient *I*–*t* curves of different-sized In_2S_3. Generally, strong photocurrent response under illumination implies high separation efficiency of the charge carrier. Among the three samples, In_2S_3-10 exhibited the highest photocurrent density, which was about three times that of the other two samples, indicating that the material was highly efficient in separating the photogenerated electron–hole pairs. It was noted that the photocurrent of three samples came back rapidly to zero once the light was switched off. Good reproducibility of the photocurrent suggested the rapid photoresponse and recovery properties of the as-synthesized photocatalysts.

EIS was performed to evaluate the charge transfer resistance of In_2S_3-5, In_2S_3-10, and In_2S_3-15 (as shown in Fig. 6d). The diameter of the semicircle (or arc) in the Nyquist plots at high frequency provided the information on the charge transfer, typically, small diameter represented the low charge transfer resistance (R_{ct}).[35] Obviously, In_2S_3-10 displayed the lowest R_{ct} in three samples, indicating the fastest charge transfer rate from the photocatalyst to the photoelectrode,[36] which was beneficial to the electron–hole separation.

3.2.4 Surface property. The specific surface areas of the catalysts are important to determine their photocatalysis. Large specific surface areas not only afforded more interface active sites between photocatalysts and the dye molecules for effective adsorption but also enhanced charge separation efficiency to produce more oxidant radicals.[11] Fig. 7 is the N_2 adsorption–desorption isotherm of different-sized In_2S_3. The adsorption curves displayed hysteresis loops in the range of 0.45–0.99 P/P_0 and presented type IV isotherms, which were identified as characteristic of mesoporous materials.[37] The mesoporous structures originated from the space among the interleaved nanoflakes, indirectly evidencing that the as-synthesized In_2S_3 were hierarchically constructed.[37] The pore size distribution was within 3–120 nm (using BJH analysis), typically presenting a bimodal shape with two maxima at ~3.8 and ~31 nm (insets to Fig. 7a–c). The pore size distribution at ~3.8 nm is possibly attributed to the formed funnel-like pores by the interleaved nanoflakes in the centre of thornball-like structures,[38] while that at ~31 nm originated from the intervals among the nanoflakes. In_2S_3-10 had a slightly smaller pore size (31.45, 30.54, and 31.40 nm for In_2S_3-5, In_2S_3-10 and In_2S_3-15, respectively), indicating that nanoflakes were stacked tightly with small intervals, in accordance with a slightly lower adsorption amount in the high pressure region (Fig. 7b). Quantitative calculation showed that the BET surface area decreased with In_2S_3 size increasing (34.26, 26.17 and 20.73 $m^2\ g^{-1}$ for In_2S_3-5, In_2S_3-10 and In_2S_3-15, respectively).

Besides the specific surface areas, the groups adsorbed on the surface of catalysts which impact the hydrophilicity and surface charge also influence the catalysis. FT-IR spectra were recorded to probe the surface groups of the three samples (as shown in Fig. 8a). The peak at 806 cm^{-1} corresponding to the In–S vibration peak[39,40], and that at 476 cm^{-1} corresponding to the In–O vibration peak[41,42] were observed in all three samples. The presence of In–O vibration originated from the interaction of In^{3+} with the oxygen-containing surface functional groups in CA molecules.[43] Compared to In_2S_3-5 and In_2S_3-15, In_2S_3-10 displayed stronger peaks of ν(O–H) at 3425 cm^{-1}, 1627 cm^{-1} and ν(In–O–C) at 1078 cm^{-1},[24] respectively, indicating that –OH groups were the main adsorbed surface groups. The presence of –OH groups from CA molecules confirmed that the generation of In_2S_3 was originated from the decompostion of In-CA compound.

Next, zeta potential, which is deemed as an indicator for the surface charge of the solid particles was measured. Zeta potential values of In_2S_3-5, In_2S_3-10 and In_2S_3-15 were −15.32, −18.25 and −13.63 mV, respectively (as shown in Fig. 8b). The negative

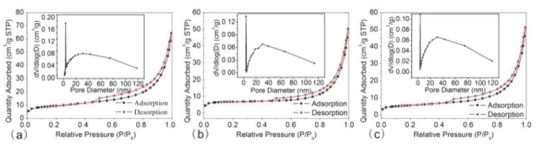

Fig. 7 Nitrogen adsorption–desorption curves of In_2S_3-5 (a), In_2S_3-10 (b), and In_2S_3-15 (c) (the insets show the pore size distribution curves).

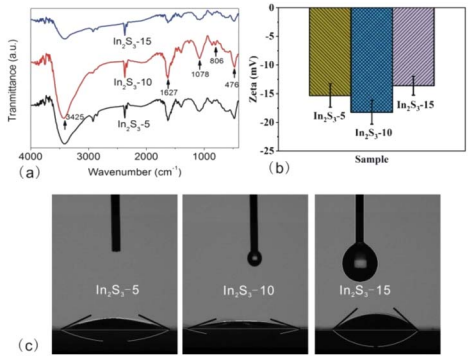

Fig. 8 FT-IR spectra (a), zeta potential (b), and water contact angle measurements (c) of In_2S_3-5, In_2S_3-10, and In_2S_3-15.

charge taken on the surface was related to the adsorption of –OH groups on the surface. In_2S_3-10 had the most negative charges on its surface, indicating that lots of –OH groups were adsorbed. Finally, surface hydrophilicity of different-sized In_2S_3 samples were quantified from water contact angle measurements. Fig. 8c shows the contact angles of In_2S_3-5, In_2S_3-10 and In_2S_3-15 to be 24.85°, 14.38° and 42.39°, respectively. Obviously, three In_2S_3 presented hydrophilicity, in particular, In_2S_3-10 presented the maximum hydrophilicity, which was connected with more adsorbed –OH groups based on the complementary effects of the specific surface area and crystallinity.

3.3 Photocatalysis

3.3.1 The photodegradation of RhB with different-sized In_2S_3. As a semiconductor with a narrow band gap, In_2S_3 can be used as the photocatalyst. RhB was selected as the dye to measure the photocatalysis of In_2S_3. Fig. 9a shows the concentration decrease of RhB (characterized by C_t/C_0) as a function of the reaction time. C_0 and C_t corresponded to the maximum absorbance of RhB at the original and particular moment, respectively. Before the photodegradation, the suspension was kept in the dark for 30 minutes. During the initial 10 minutes, the absorbance decrease was relatively high, then it was almost not changing. We used $(C_t - C_0)/C_0$ during this period to represent the adsorption efficiency (ADE). Obviously, In_2S_3-10 displayed the highest ADE, which was possibly connected with the strongest hydrophilicity and most negative charges taken. With the light on, the concentration of RhB went on decreasing. Using a similar formula to obtain the photodegradation efficiency (PDE), In_2S_3-10 displayed a maximum PDE of up to 99.99%, just after 25 min of illumination, much higher than that previously reported with the similarly structured In_2S_3 (as shown in Table 2). As a comparison, the concentration change of RhB without In_2S_3 only displayed 2.34% absorbance attenuation under illumination. Obviously, In_2S_3 as the catalyst can photodegrade RhB efficiently.

Next, we measured the photodegradation of RhB during the photoreaction (Fig. 9b). It was approximately fitted with the liner equation of $\ln(C_t/C_0) = -kt$ and the obtained R^2 value was over 0.9, suggesting that the photodegradation reaction meets the pseudo-first-order kinetics as a function of the time. From the equation, the k value was obtained easily. With the size of In_2S_3 increasing, the k value increased first and then decreased largely. In_2S_3-10 showed the maximum k value up to 0.25 min^{-1}, probably, the fastest rate in the photodegradation of RhB.

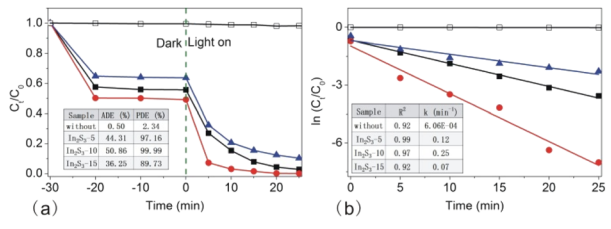

Fig. 9 Photodegradation of RhB without In_2S_3 (□), with In_2S_3-5 (■), In_2S_3-10 (●), In_2S_3-15 (▲) (a) and the corresponding plots of $\ln(C_t/C_0)$ *versus* irradiation time (b), the insert tables to (a) and (b) show adsorption efficiency (ADE), photodegradation efficiency (PDE) and correlation coefficient (R^2), rate constant (k) of different samples.

3.3.2 Photodegradation path. Mass spectra (MS) were collected to determine the photodegradation products of RhB. Fig. 10a shows the influence of the illumination time on the product of RhB in the case of In_2S_3-5. It showed the peak of the RhB matrix at $m/z = 443$ at the initial moment. With the illumination time increasing to 5 min, more peaks appeared with increased abundance in the range of $m/z = 250$–400. Furthermore, when the illumination time increased to 20 min, not only did the peaks in the range of $m/z = 250$–400 increase but also the peaks in the range of $m/z = 50$–150 increased with higher abundance. Obviously, with photoreaction time increasing, more and more small molecules with higher abundance appeared, indicating RhB was decomposed but not adsorbed by In_2S_3. Fig. 10b displayed the photodegradation product of RhB using different In_2S_3 as photocatalysts after 20 min of the illumination time. The abundance of small molecules instead of RhB matrix became relatively stronger in those systems containing In_2S_3-5, especially In_2S_3-10. However, the RhB matrix kept a relatively strong abundance in the system containing In_2S_3-15. These facts confirmed that In_2S_3-5 and In_2S_3-10, especially In_2S_3-10 almost decomposed RhB completely after 20 minutes of illumination.

Next, we speculated several possible photodegradation path from the RhB matrix to small molecular products. (1) Firstly, RhB experienced a series of de-ethylation reactions, such as from $m/z = 443$ to $m/z = 415$, 387.[29] Next, the intermediates were attacked by ˙OH, followed by the removal of $–NH_2$ and the addition of –OH (from $m/z = 387$ to $m/z = 362$), then the gradual removal of –OH (from $m/z = 362$ to $m/z = 345$, 329). (2) ˙OH attacked the xanthene ring, followed by the ring opening, the removal of $–N(C_2H_5)_2$, and the addition of –OH ($m/z = 443$ to $m/z = 334$),[44] then the removal of –OH ($m/z = 334$ to 318, 302). Next, the carboxyl groups were removed partially from the xanthene ring after the loss of all ethyl groups ($m/z = 302$ to $m/z = 290$), followed by the removal of –OH ($m/z = 290$ to $m/z = 274$). (3) The intermediate product at $m/z = 318$ experienced a ring-opening reaction and the rupture of carbon–carbon bonds ($m/z = 318$ to $m/z = 262$),[44] followed by the gradual removal of –OH groups (from $m/z = 262$ to $m/z = 246$, 230). (4) The intermediate at $m/z = 262$ removed the –COOH groups ($m/z = 262$ to $m/z = 218$) directly,[44] followed by the removal of $–NH_2^+$ ($m/z = 218$ to $m/z = 205$). Finally, all of the obtained residues further decomposed to small molecules ($m/z = 149$, $m/z = 116$, $m/z = 74$, $m/z = 65$) through the ring-opening reactions.[29,45–47] According to the above results, we speculated the possible path of RhB photodegradation (as shown in Fig. 10c).

3.3.3 Photodegradation mechanism. It is well-known that the active species in a photodegradation reaction is ˙OH (originating from the combination of holes with H_2O or OH^-) and $˙O_2^-$ (originating from the combination of electrons with O_2) to oxidize dye molecules at the active sites. The indirect detection of active species for the photodegradation mechanism by the use of scavengers has been confirmed in many reports.[48,49] Similar to those in previous literatures,[50,51] isopropyl alcohol (IPA), benzoquinone (BQ), and triethanolamine (TEOA) as the scavengers

Table 2 The reported efficiency and tested conditions of In_2S_3 from previous literature

Catalyst	Light source	Time (min)	Degradation rate (%)	Reference
In_2S_3-10	300 W Xe lamp	25	99.9	This work
In_2S_3	500 W Xe lamp	60	97.5	25
Ca^{2+} doped In_2S_3	300 W Xe lamp	100	99.9	23
YTIS-4	300 W Xe lamp	100	98.4	22
In_2S_3/5G	300 W Xe lamp	180	99.23	24
Ag: In_2S_3 (2)	150 W Xe lamp	180	99.5	26

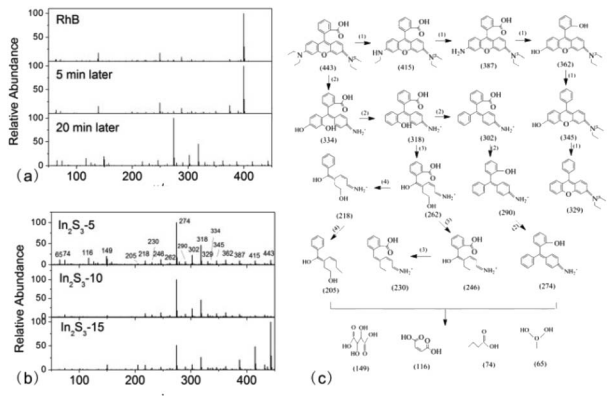

Fig. 10 MS of RhB photodegradation products with In_2S_3-5 as the photocatalysts for 0 min, 5 min and 20 min (a) MS of RhB photodegradation products with In_2S_3-5, In_2S_3-10 and In_2S_3-15 as photocatalysts for 20 min (b) and the possible photodegradation path of RhB (c).

were added to the system to verify the presence of $^{\bullet}OH$, $^{\bullet}O_2^-$ and h^+, respectively. Fig. 11a shows the change in the photodegradation of RhB with In_2S_3-10 as the photocatalyst after the addition of scavengers. Not only TEOA but BQ also suppressed the photodegradation greatly, implying that h^+ and $^{\bullet}O_2^-$ were the active specifies, which was attributed to the relative potential. The potential of holes (+1.28 eV, E_{VB} in Table 1) was more negative than φ ($H_2O/^{\bullet}OH$) (+2.68 eV) or φ ($OH^-/^{\bullet}OH$) (+1.99 eV), which was unable to oxidize H_2O or OH^- to $^{\bullet}OH$. However, the potential of electrons (−0.88 eV, E_{CB} in Table 1) was more negative than φ ($O_2/^{\bullet}O_2^-$) (−0.33 V), which was effective to make O_2 into $^{\bullet}O_2^-$. Therefore, h^+ and $^{\bullet}O_2^-$ were the active specifies. Note that, although h^+ could not oxidize H_2O to $^{\bullet}OH$ directly, the protonation of $^{\bullet}O_2^-$ into H_2O_2 followed by its decomposition resulted in the generation of bits of $^{\bullet}OH$ inevitably.[52] Compared to In_2S_3-5 and In_2S_3-15, In_2S_3-10 produced more electrons and holes owing to higher electron–hole separation (as shown in Fig. 6), contributing to the participation of more active specifies in the reaction for faster photodegradation rate.

The active site is one more factor influencing the photocatalysis reaction, which is connected to interfacial adsorption. Next, we carried out the photodegradation of different dye molecules with In_2S_3-10 as the photocatalyst (as shown in Fig. 11b). Clearly, In_2S_3-10 displayed excellent photodegradation of cationic dyes such as RhB, MG, and CV. However, it showed poor photodegradation of anionic dyes such as MO, CR, and AR. It is especially noteworthy that In_2S_3 displayed high ADE for three cationic dyes, therefore, the excellent photodegradation was reasonably attributed to the adsorption of –OH groups on the surface of In_2S_3-10 for the increased hydrophilicity and surface negative charges to afford more reaction active sites. High ADE resulted in high substrate concentration for efficient decomposition of the adsorbed molecules.

Finally, we observed the colour change of the photocatalyst and substrate before and after the illumination. In the dark, the significantly darker colour of In_2S_3-10 confirmed that RhB was adsorbed on its surface. After turning on the light, In_2S_3-10 changed back to its original colour, indicating that the absorbed RhB on the surface of photocatalysts decomposed completely (as shown in the inset to Fig. 11c on the right). At the same time, RhB faded slightly in the dark, however, it turned colourless quickly after turning on the light (as shown in the inset in Fig. 11c on the left). The change in the absorption spectrum also clearly demonstrated the same results (Fig. 11c). Keeping it in the dark for initial 30 min, the peak intensity decreased without shifting of the peak position. However, after illumination for 5 min to 25 min, peak intensity decreased significantly with the gradual hypsochromic shifting of the peak

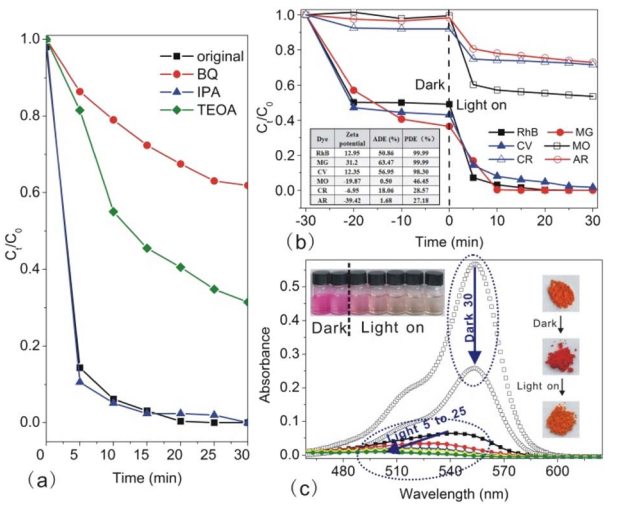

Fig. 11 Photodegradation of RhB with In_2S_3-10 as the photocatalyst after the addition of different scavengers (a), photodegradation of different dyes with In_2S_3-10 as the photocatalyst (b) and absorption spectrum of RhB at different moments (c), the insets on the left and right represent the colour change of RhB solution and In_2S_3-10, respectively.

position from 554 nm to 498 nm, which was caused by the step-by-step *N*-deethylation of RhB,[53] implying that RhB matrix was decomposed by In_2S_3.

3.3.4 Reusability. As a catalyst, long-term stability is required to be considered in practical applications. Based on the excellent photocatalysis of In_2S_3-10, we carried out the photodegradation of RhB in 5 sequential cycles (as shown in Fig. 12a). With the reused times of In_2S_3-10 increasing, ADE decreased gradually, resulting in decreased PDE in the initial 25 min. A similar phenomenon has been reported in previous literature.[54] If the illumination time was prolonged, PDE increased obviously as it improved from 74.96% to 95.94% in the case of In_2S_3-10 after recycling 5 times. To detect the influence of the adsorbed molecules on the property of photocatalysts, we carried out SEM image of 5-time recycled and used In_2S_3-10 after 25 min of illumination (as shown in Fig. 12b). Different from 500–600 nm distinct thornball-like structures assembled by thin nanoflakes in Fig. 2b, 5-time recycled In_2S_3-10 showed such ambiguous edges that one could barely distinguish the nanoflakes. Moreover, we measured N_2 adsorption–desorption isotherms (Fig. 12c). Compared to the isotherm shown in Fig. 7b for the original In_2S_3-10 with a BET surface area of 26.17 $m^2\ g^{-1}$ and maximum pore size of 30.54 nm, 5-time recycled and used In_2S_3-10 displayed a smaller BET surface area of 11.87 $m^2\ g^{-1}$ and wider pore size distribution map without the maximum peak. Moreover, the hysteresis loop was invisible, indicating that the mesoporous among thornball-like structures disappeared, very likely to be filled by RhB molecules. The adsorbed high concentration of RhB on the surface of photocatalysts led to disabling adsorption of RhB in the solution, therefore, the deactivation of the reused In_2S_3 in the photodegradation of RhB was closely related to the reduction of the adsorption content.[54] With the adsorbed RhB on the surface of photocatalysts decomposing after the illumination, RhB in the solution was further adsorbed onto the photocatalysts for decomposition. In our next work, we will try to carry out surface treatments on the reused photocatalysts to improve the adsorption of dye molecules for increased reusability.

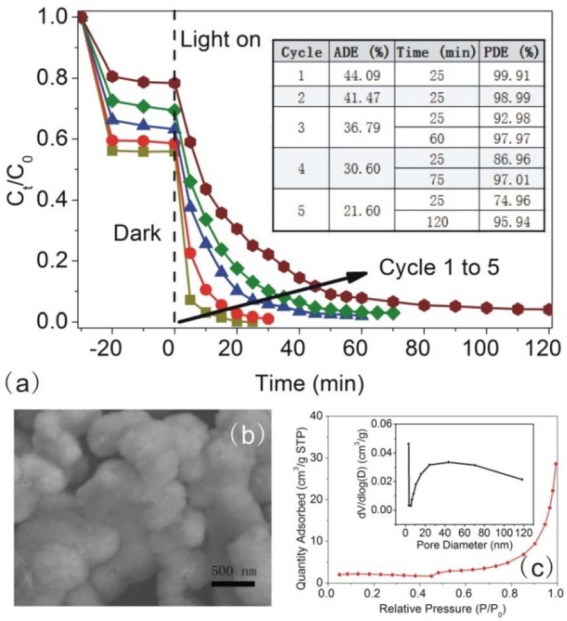

Cycle	ADE (%)	Time (min)	PDE (%)
1	44.09	25	99.91
2	41.47	25	98.99
3	36.79	25	92.98
		60	97.97
4	30.60	25	86.96
		75	97.01
5	21.60	25	74.96
		120	95.94

Fig. 12 RhB photodegradation with In_2S_3-10 as the photocatalyst in sequential 5 cycles (a), the table inside (a) displayed the photodegradation efficiency of RhB for different cycle times with different illumination time, SEM (b) and nitrogen adsorption–desorption curve (c) of In_2S_3-10 after the photodegradation for 5 cycles, the inset to (c) was the pore size distribution curve.

4 Conclusions

A facile synthesis method for different-sized thornball-like In_2S_3 with controllable photocatalysis was reported. Three In_2S_3 samples within the pore size of 400–800 nm were synthesized rapidly by one-pot microwave irradiation method at low temperature in an aqueous solution. Different-sized tetragonal β-In_2S_3 assembled by nanoflakes displayed obviously different charge separation abilities and surface properties, resulting in various photodegradation rates of RhB. In_2S_3-10 showed maximum electron–hole separation efficiency and surface attraction, contributing to the complete photodegradation of RhB in just 25 min of illumination, which was possibly the fastest rate as far as we know. The extremely rapid photodegradation was attributed to the strong adsorption of dye molecules on the In_2S_3 surface followed by its highly effective decomposition on the substrate. MS results showed that small molecules generated after RhB experienced the process of deethylation, ring-opening of xanthene, and rupture of carbon–carbon bonds. Additionally, In_2S_3-10 displayed comparable reusability only by prolonging the illumination time.

Author contributions

Chaofan Zheng: methodology, investigation; Ziyao Wang: writing-the original draft; Jialong Yuan and Xiaoyi Lu: formal analysis; Qingfeng Xu and Haixin Li: validation; Jiangang Gao: reviewing and editing; Wenjin Yue: conceptualization, supervision, funding acquisition.

Conflicts of interest

There are no conflicts to declare.

Acknowledgements

This work was supported by Universities' Scientific Research Projects in Anhui Province (KJ2021A0498), Anhui Laboratory of Clean Energy Materials and Chemistry for Sustainable Conversion of Natural Resources (LCECSC-02), and the National Undergraduate Innovation Entrepreneurship Project in Local University (20221036306).

Notes and references

1 Y. Yuan, R.-t. Guo, L.-f. Hong, X.-y. Ji, Z.-d. Lin, Z.-s. Li and W.-g. Pan, *Mater. Today Energy*, 2021, **21**, 100829.

2 J. Arun, S. Nachiappan, G. Rangarajan, R. P. Alagappan, K. P. Gopinath and E. Lichtfouse, *Environ. Chem. Lett.*, 2022, 1.
3 K. Yang, Z. Yang, C. Zhang, Y. Gu, J. Wei, Z. Li, C. Ma, X. Yang, K. Song, Y. Li, Q. Fang and J. Zhou, *Chem. Eng. J.*, 2021, **418**, 129344.
4 P. Li and T. He, *J. Mater. Chem. A*, 2021, **9**, 23364.
5 X. Li, J. Yu and M. Jaroniec, *Chem. Soc. Rev.*, 2016, **45**, 2603.
6 J. Zhang, H. Wang, X. Yuan, G. Zeng, W. Tu and S. Wang, *J. Photoch. Photobio. C*, 2019, **38**, 1.
7 W. Gao, W. Liu, Y. Leng, X. Wang, X. Wang, B. Hu, D. Yu, Y. Sang and H. Liu, *Appl. Catal., B*, 2015, **176–177**, 83.
8 N. Yahya, F. Aziz, N. A. Jamaludin, M. A. Mutalib, A. F. Ismail, W. N. W. Salleh, J. Jaafar, N. Yusof and N. A. Ludin, *J. Environ. Chem. Eng.*, 2018, **6**, 7411.
9 L. Qi, H. Li and L. Dong, *Mater. Lett.*, 2013, **107**, 354.
10 A. K. Nayak, S. Lee, Y. Sohn and D. Pradhan, *CrystEngComm*, 2014, **16**, 8064.
11 C. Wei, W. Guo, J. Yang, H. Fan, J. Zhang and W. Zheng, *RSC Adv.*, 2014, **4**, 50456.
12 T. Li, S. Zhang, S. Meng, X. Ye, X. Fu and S. Chen, *RSC Adv.*, 2017, **7**, 6457.
13 L. Liu, W. Xiang, J. Zhong, X. Yang, X. Liang, H. Liu and W. Cai, *J. Alloys Compd.*, 2010, **493**, 309.
14 R. Amutha, S. Akilandeswari, B. Ahmmad, M. Muruganandham and M. Sillanpaa, *J. Nanosci. Nanotechnol.*, 2010, **10**, 8438.
15 S. Rengaraj, S. Venkataraj, C.-w. Tai, Y. Kim, E. Repo and M. Sillanpää, *Langmuir*, 2011, **27**, 5534.
16 X. Sheng, L. Wang, G. Chen and D. Yang, *J. Nanomater.*, 2011, **2011**, 280216.
17 B. Xue, F. Xu, B. Wang and A. Dong, *CrystEngComm*, 2016, **18**, 250.
18 P. L. Saldanha, V. Lesnyak and L. Manna, *Nano Today*, 2017, **12**, 46.
19 Z. Pang, M. Zhang, L. Huang, R. Wen, J. Lu, Y. Zhao, A. Wei, L. Tao, D. Luo, J. Liu, Y. Yang, Y. Xiao and Z. Xiao, *Mater. Lett.*, 2018, **210**, 66.
20 S. D. Naik, T. C. Jagadale, S. K. Apte, R. S. Sonawane, M. V. Kulkarni, S. I. Patil, S. B. Ogale and B. B. Kale, *Chem. Phys. Lett.*, 2008, **452**, 301.
21 C. R. Patra, S. Patra, A. Gabashvili, Y. Mastai, Y. Koltypin, A. Gedanken, V. Palchik and M. A. Slifkin, *J. Nanosci. Nanotechnol.*, 2006, **6**, 845.
22 Z. Wu, X. Yuan, G. Zeng, L. Jiang, H. Zhong, Y. Xie, H. Wang, X. Chen and H. Wang, *Appl. Catal., B*, 2018, **225**, 8.
23 S. Yang, C. Y. Xu, B. Y. Zhang, L. Yang, S. P. Hu and L. Zhen, *J. Colloid Interface Sci.*, 2017, **491**, 230.
24 L. Chen, G. Yang, X. Wei, H. Xu and S. Jin, *J. Alloys Compd.*, 2022, **895**, 162589.
25 W. Wang, W. Zhu and L. Zhang, *Res. Chem. Intermed.*, 2009, **35**, 761.
26 S. Alhammadi, B. G. Mun, S. Gedi, V. R. Minnam Reddy, A. M. Rabie, M. S. Sayed, J.-J. Shim, H. Park and W. K. Kim, *J. Mol. Liq.*, 2021, **344**, 117649.
27 Q. Xu, C. Zheng, Z. Wang, Z. Zhang, X. Su, B. Sun, G. Nie and W. Yue, *J. Mater. Sci.*, 2022, **57**, 7531.
28 Q. Xu, Z. Wang, H. Yang, Y. Xiang, G. Nie and W. Yue, *J. Alloys Compd.*, 2022, **904**, 163966.
29 W. Yue, Z. Wang, J. Gong, Z. Wang and Y. Dong, *Mater. Sci. Semicond. Process.*, 2021, **126**, 105671.
30 P. Makula, M. Pacia and W. Macyk, *J. Phys. Chem. Lett.*, 2018, **9**, 6814.
31 H. Zhong, S. S. Lo, T. Mirkovic, Y. Li, Y. Ding, Y. Li and G. D. Scholes, *ACS Nano*, 2010, **4**, 5253.
32 J. Xu, C. Liu, J. Niu and M. Chen, *Sep. Purif. Technol.*, 2020, **230**, 115861.
33 Q. Wang, J. Huang, H. Sun, K.-Q. Zhang and Y. Lai, *Nanoscale*, 2017, **9**, 16046.
34 J. Chang and E. R. Waclawik, *RSC Adv.*, 2014, **4**, 23505.
35 S. B. Kokane, R. Sasikala, D. M. Phase and S. D. Sartale, *J. Mater. Sci.*, 2017, **52**, 7077.
36 R. He, K. Xue, J. Wang, T. Yang, R. Sun, L. Wang, X. Yu, U. Omeoga, W. Wang, T. Yang, Y. Hu and S. Pi, *J. Mater. Sci.*, 2019, **54**, 14690.
37 J. Chen, W. Liu and W. Gao, *Appl. Surf. Sci.*, 2016, 368.
38 L.-Y. Chen, Z.-D. Zhang and W.-Z. Wang, *J. Phys. Chem. C*, 2008, **112**, 4117.
39 J. Parhizkar and M. R. M. Shafiee, *Nanochem. Res.*, 2020, **5**, 168.
40 N. M. Huang, *J. Nanomater.*, 2011, **2011**, 815709.
41 X. Yuan, L. Jiang, J. Liang, Y. Pan, J. Zhang, H. Wang, L. Leng, Z. Wu, R. Guan and G. Zeng, *Chem. Eng. J.*, 2019, **356**, 371.
42 C. Chen, D. Chen, X. Jiao and C. Wang, *Chem. Commun.*, 2006, 4632.
43 P. Berki, Z. Németh, B. Réti, O. Berkesi, A. Magrez, V. Aroutiounian, L. Forró and K. Hernadi, *Carbon*, 2013, **60**, 266.
44 J. Wu, N. Qin, E. Lin, B. Yuan, Z. Kang and D. Bao, *Nanoscale*, 2019, **11**, 21128.
45 Y. A. B. Neolaka, Z. S. Ngara, Y. Lawa, J. N. Naat, D. Prasetyo Benu, A. Chetouani, H. Elmsellem, H. Darmokoesoemo and H. Septya Kusuma, *J. Environ. Chem. Eng.*, 2019, **7**, 103482.
46 M. Rakibuddin, S. Gazi and R. Ananthakrishnan, *Catal. Commun.*, 2015, **58**, 53.
47 S. Vigneshwaran, C. M. Park and S. Meenakshi, *Sep. Purif. Technol.*, 2021, **258**, 118003.
48 A. Das, M. K. Adak, N. Mahata and B. Biswas, *J. Mol. Liq.*, 2021, **338**, 116479.
49 V. H. Nguyen, L. A. Phan Thi, P. S. Chandana, H. T. Do, T. H. Pham, T. Lee, T. D. Nguyen, C. Le Phuoc and P. T. Huong, *Chemosphere*, 2021, 276.
50 T. D. Munusamy, C. S. Yee and M. M. R. Khan, *Adv. Powder Technol.*, 2020, **31**, 2921.
51 H. Wang, Z. Ye, C. Liu, J. Li, M. Zhou, Q. Guan, P. Lv, P. Huo and Y. Yan, *Appl. Surf. Sci.*, 2015, **353**, 391.
52 A. Ajmal, I. Majeed, R. N. Malik, H. Idriss and M. A. Nadeem, *RSC Adv.*, 2014, **4**, 37003.
53 J. Zhuang, W. Dai, Q. Tian, Z. Li, L. Xie, J. Wang, P. Liu, X. Shi and D. Wang, *Langmuir*, 2010, **26**, 9686.
54 S. Ge, L. Cai, D. Li, W. Fa, Y. Zhang and Z. Zheng, *J. Nanopart. Res.*, 2015, **17**, 488.